

Nucleon-induced reactions at intermediate energies: New data at 96 MeV and theoretical status

V. Blideanu^{1*}, F. R. Lecolley¹, J. F. Lecolley¹, T. Lefort¹, N. Marie¹, A. Ataç², G. Ban¹, B. Bergenwall², J. Blomgren², S. Dangtip^{2,3}, K. Elmgren⁴, Ph. Eudes⁵, Y. Foucher⁶, A. Guertin⁵, F. Haddad⁵, A. Hildebrand², C. Johansson², O. Jonsson⁷, M. Kerveno⁸, T. Kirchner⁵, J. Klug², Ch. Le Brun⁹, C. Lebrun⁵, M. Louvel¹, P. Nadel-Turonski¹⁰, L. Nilsson^{2,7}, N. Olsson^{2,4}, S. Pomp², A. V. Prokofiev⁷, P.-U. Renberg⁷, G. Rivière⁵, I. Slypen¹¹, L. Stuttgé⁸, U. Tippawan^{2,3}, M. Österlund²

¹*LPC, ENSICAEN, Université de Caen, CNRS/IN2P3, Caen, France*

²*Department of Neutron Research, Uppsala University, Sweden*

³*Fast Neutron Research Facility, Chiang Mai University, Thailand*

⁴*Swedish Defence Research Agency, Stockholm, Sweden*

⁵*SUBATECH, Université de Nantes, CNRS/IN2P3, France*

⁶*DSM/DAPNIA/SPhN, CEA Saclay, Gif-sur-Yvette, France*

⁷*The Svedberg Laboratory, Uppsala University, Sweden*

⁸*IReS, Strasbourg, France*

⁹*Laboratoire de Physique Subatomique et de Cosmologie, Grenoble, France*

¹⁰*Department of Radiation Sciences, Uppsala University, Sweden and*

¹¹*Institut de Physique Nucléaire, Université Catholique de Louvain, Louvain-la-Neuve, Belgium*

Double-differential cross sections for light charged particle production (up to $A = 4$) were measured in 96 MeV neutron-induced reactions, at TSL laboratory cyclotron in Uppsala (Sweden). Measurements for three targets, Fe, Pb, and U, were performed using two independent devices, SCANDAL and MEDLEY. The data were recorded with low energy thresholds and for a wide angular range (20 – 160 degrees). The normalization procedure used to extract the cross sections is based on the np elastic scattering reaction that we measured and for which we present experimental results. A good control of the systematic uncertainties affecting the results is achieved. Calculations using the exciton model are reported. Two different theoretical approaches proposed to improve its predictive power regarding the complex particle emission are tested. The capabilities of each approach is illustrated by comparison with the 96 MeV data that we measured, and with other experimental results available in the literature.

PACS numbers: 24.10.-i, 25.40.-h, 28.20.-v

I. INTRODUCTION

The deep understanding of nucleon-induced reactions is a crucial step for the further development of nuclear reactions theory in general. In addition, a complete information in this field is strongly needed for a large amount of applications, such as the incineration of nuclear waste with accelerator-driven systems (ADS), cancer therapy or the control of radiation effects induced by terrestrial cosmic rays in microelectronics. For this reason, the problem of nucleon-induced reactions has gained a renewed interest in the last few years. This interest has been expressed in part by extensive experimental campaigns, such as, for example, those carried out by several laboratories in Europe in the framework of the HINDAS program [1].

Particularly, nucleon-induced reactions in the 20-200 MeV energy range, have for a long time been the subject of intensive theoretical studies. For this range, the first major step for the improvement of nuclear reaction models consisted of the introduction of the so-called "pre-equilibrium process". This process has been proposed in

order to explain the smooth dependence of the particle emission probability versus angle and energy, which has been observed experimentally. This "pre-equilibrium" process is supposed to occur at an intermediate stage and to consist of multiple nucleon-nucleon interactions which take place inside the target nucleus. During that process, particle emission occurs after completion of the one-step interaction phase, i.e., direct process phase, but a long time before the statistical equilibrium of the compound nucleus has been reached.

During the last 40 years, several approaches attempted to give a theoretical description of this pre-equilibrium process. Some of them have shown all along a good predictive power for a wide set of experimental energy distributions of nucleons emitted in nucleon-nucleus reactions. However, those models were unable to reproduce the experimental distributions of complex particles, for which they systematically underestimate the production rates. Among them, the exciton model of Griffin [2] is a very good example. Originally introduced in 1966, this model has been quickly adopted by the community because of its adaptability and simplicity. In an attempt to increase its capability in reproducing the complex particle rates, two main approaches have been developed. The first one, proposed in 1973 [3], introduces a cluster formation prob-

*blideanu@lpccaen.in2p3.fr

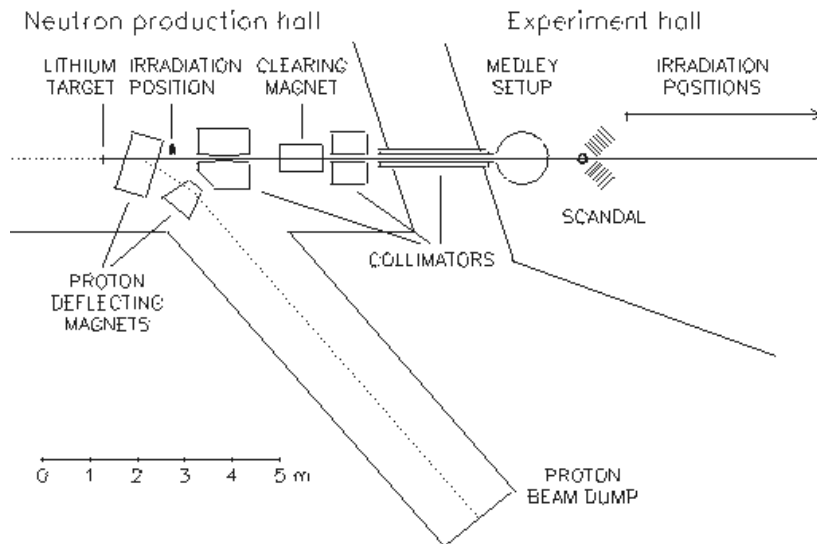


FIG. 1: TSL neutron beam facility and the location of the detection systems used in the experiment.

ability during the nucleon-nucleon interactions inside the nucleus. The second one formulated by Kalbach in 1977 [4] is a completely different approach which takes into account the possible contributions of direct pick-up and knock-out mechanisms.

Nowadays, the exciton model modified according to these theories is the only one available to calculate energy spectra of both nucleons and complex particles emitted in nucleon-induced reactions at intermediate energies. In the past, both approaches have been tested against data, and they both show a satisfactory agreement with experimental distributions [4, 5]. The comparisons were made using the data available at that moment and which concern a limited number of reaction configurations and incident energies, lower than 63 MeV. Despite this success, several questions are still open to discussion. An extended study of the influence of the entrance channel parameters is necessary, i.e. the dependence on the incident particle type and on the incident energy has to be investigated.

The measurements presented in this work are part of the HINDAS program and they concern double-differential distributions of light charged particles, up to $A = 4$, emitted in 96 MeV neutron induced reactions on three targets, iron, lead and uranium. Calculations for those reactions are performed with the basic exciton model implemented in the GNASH code [6], and with both independent approaches proposed respectively by Ribanský-Obložinský [3] and by Kalbach [4]. The robustness of those approaches are also tested for other reactions with incident protons at lower energies and with other targets for which experimental results are available in the literature. This study allows a global view on the predictive power of each model.

The experimental set-up used for the data taking is briefly presented in section II. In section III, details con-

cerning the procedures used to obtain the energy spectra and the cross section normalization are given. The results are presented in section IV. Section V is dedicated to the description of the theoretical calculations related to the particle emission in nucleon-induced reactions at intermediate energies, and the predictions of the models are compared to experimental data. The conclusions of this work are given in section VI.

II. EXPERIMENTAL PROCEDURE

The experiments were performed using the neutron beam available at the TSL laboratory in Uppsala (Sweden) whose facility is presented in Fig. 1. Neutrons were produced by ${}^7\text{Li}(p,n){}^7\text{Be}$ reactions using a 100 MeV proton beam impinging on a lithium target. The beam monitoring was provided by a Faraday cup where the proton beam was dumped and by a fission detector composed of thin-film breakdown counters [7] placed in the experimental hall. The stability of the beam was checked regularly during the data taking. The deviations found between the indications of both monitors did not exceeded 2 %.

Difficulties encountered when working with neutron beams are related to their characteristics. The neutrons of the beam are not strictly mono-energetic. This is illustrated in Fig. 2(a) where a typical neutron spectrum is shown. It presents two components: one is a peak centered at an energy slightly lower than the incident proton beam energy ($Q = -1.6\text{MeV}$), diminished of the energy loss inside the production target, and the other is a low energy tail which contains about 50 % of the total number of produced neutrons, and which originates from highly excited states of ${}^7\text{Be}$. For the data analysis, events associated with low energy neutrons must be rejected. The method employed for this rejection will be described in

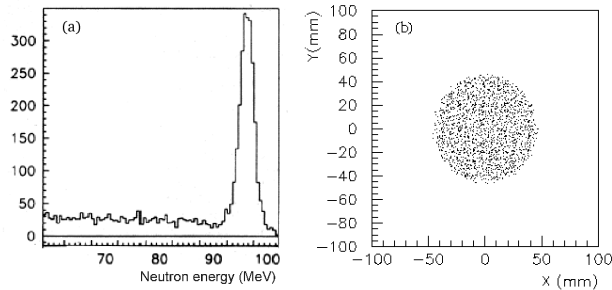


FIG. 2: (a) Neutron energy spectra resulting from a 100 MeV proton beam on a 4 mm thick lithium target. (b) Scatter plot showing the profile of the neutron beam at about 10 meters from the lithium target.

the forthcoming sections. After selection, the intensity of the resulting 96 MeV neutron beam is of the order of 10^4 n/cm²/sec. The neutron beam is collimated to a solid angle of $60 \mu\text{sr}$ and the beam spot at about 10 meters from the lithium target has a diameter of 8 cm (Fig. 2(b)). These characteristics impose the use of an adequate detection set-up in order to obtain a satisfactory counting rate, keeping, at the same time, the energy and angular resolutions within reasonable limits. Two independent detection systems, MEDLEY and SCANDAL, were used in our experiments. They were placed one after the other on the beam line as shown in Fig. 1.

A. MEDLEY set-up

The first set-up downstream the beam was the MEDLEY detection array, described in detail in reference [8]. Composed of eight Si-Si-CsI telescopes, this system is used to detect light charged particles up to $A = 4$, with a low-energy threshold and over an angular domain ranging from 20 to 160 degrees, in steps of 20 degrees. The telescopes were placed inside a vacuum reaction chamber of 100 cm diameter. The arrangement of the eight telescopes inside the chamber and a detailed view of one of them are given in Fig. 3. For the MEDLEY set-up, the reaction target was placed at the center of the chamber and was tilted 45 degrees with respect to the beam direction, in order to minimize the energy loss of the produced particles inside the target. Typically, $50 \mu\text{m}$ thick targets were used for all experiments. This allows small corrections for the energy loss of the emitted particles inside the target, but it also results in a low particle production rate. Due to the thin targets used and to the small solid angles of the telescopes, the statistics accumulated using the MEDLEY set-up is relatively poor. The angular resolution was defined by the target active area and by the opening angle subtended by each telescope. It has been estimated using Monte Carlo simulations and typical values derived are of the order of 5 degrees.

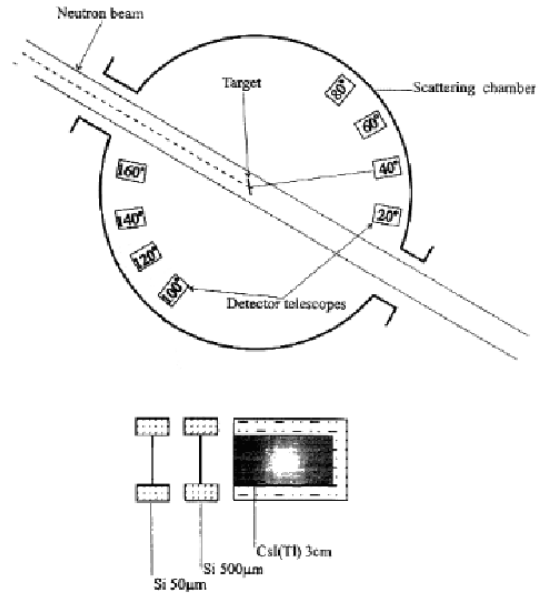


FIG. 3: MEDLEY detection array and the configuration of one telescope.

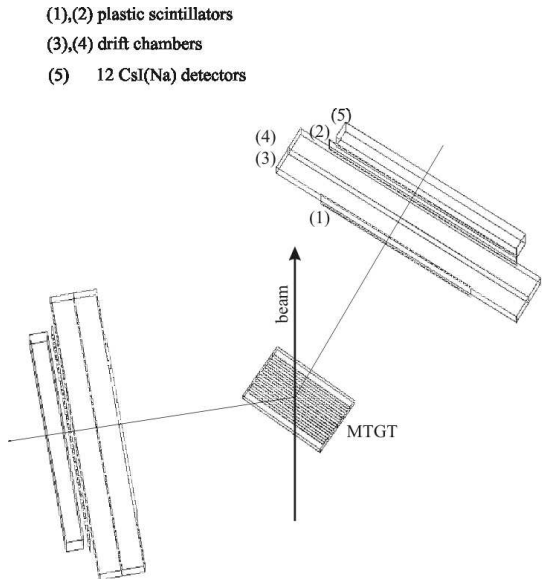


FIG. 4: Schematic view of SCANDAL set-up.

B. SCANDAL set-up

A detailed description of SCANDAL is given in reference [9]. It consists of two identical systems located on each side of the neutron beam and which covered a detection angular range of 10 – 140 degrees (Fig. 4). Since particles travel in air before entering the set-up, only protons with energies larger than 30 MeV and a small number of deuterons could be detected. Each arm was composed of two 2 mm thick plastic scintillator used

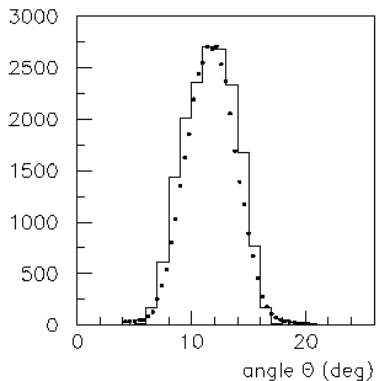


FIG. 5: Experimental distribution for emission angles of particles detected in a CsI detector (dots) compared with the simulation results (histogram).

as triggers, two drift chambers used for the particle tracking and an array of 12 CsI detectors enabling to measure particle residual energies. The emission angle of each particle was determined from its trajectory through the drift chambers. With this method, the angular resolution was estimated to be of the order of 1 degree, which was a significant improvement compared to that obtained with the MEDLEY set-up. An example of an angular distribution obtained with particles detected in one of the CsI detectors is shown, together with simulation results, in Fig. 5. The very good agreement observed demonstrates the validity of the tracking method used and the quality of the drift chambers. Using the trajectories, the coordinates of the nuclear reactions on the target plane could be determined with a back-tracking procedure. Since the SCANDAL targets were larger than the neutron beam, it was crucial to determine the active target area with good precision.

The SCANDAL set-up had the particularity to operate with a multitarget system (MTGT) [10], which allows an increase of the counting rate without impairing the energy resolution. Up to seven targets, inserted between multi-wire proportional counters (MWPC's), can be mounted simultaneously. The information given by MWPC's allows to determine the target from which the particle has been emitted, and to apply corrections to the particle energy by taking into account the energy losses inside the subsequent targets. In addition, by mounting simultaneously targets of different elements, several nuclear reactions can be studied at the same time. During our experiments, we operated with seven targets: five targets were made of the same material and dedicated to the reactions under study (iron, lead or uranium), another one was a pure carbon target and the last one was a CH₂ target. By these means, events associated to the reactions under study and events corresponding to the H(n,p) elastic scattering were recorded at the same time. As will be explained in section III.C, those events enabled to apply an unambiguous normalization procedure for the

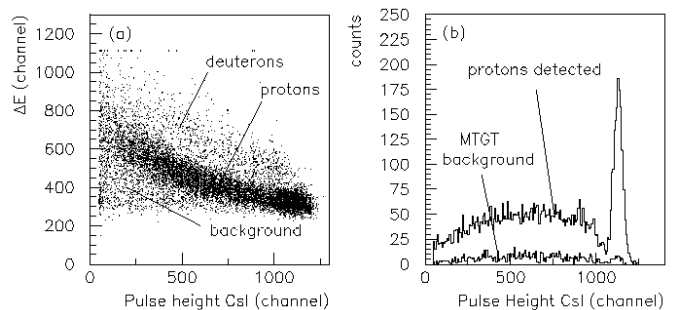


FIG. 6: (a) Two-dimensional scatter plot containing events recorded in the 10 – 11 degrees angular range using a CH₂ target. (b) Contamination in the recorded proton spectra due to reactions in the multitarget box.

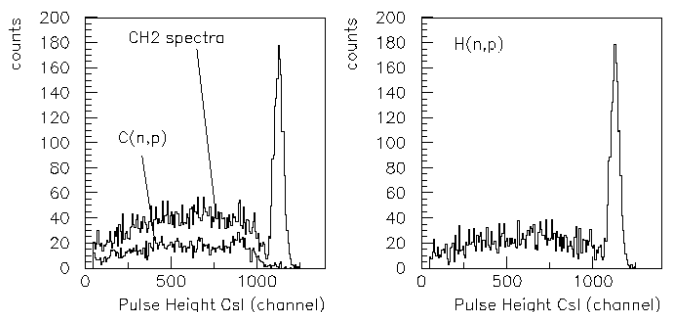


FIG. 7: Contribution of protons from the ¹²C(n,p) reaction in the CH₂ spectra (left part). On the right, the spectra of protons from the H(n,p) elastic scattering obtained after subtraction are shown.

extraction of the experimental cross sections, without requiring corrections for detection efficiencies, acquisition dead time or beam intensity.

III. DATA REDUCTION

The data recorded using both detection systems were analyzed on a event-by event basis in order to extract the energy spectra of the emitted particles. The procedures used for each set-up are described in the next two subsections. The last subsection is dedicated to the cross section normalization method.

A. Event sorting for SCANDAL set-up

The first step in the data analysis was to identify the target where the emission occurred inside the multitarget system (MTGT). It was derived from the signals given by the multi-wire proportional counters located in between the targets. Then the trajectories calculated with the drift chambers enable to determine the emission angle of the

each particle. In this way, both a target and an emission angle are associated to each recorded event.

The particle identification was made by the well known ΔE - E technique, using signals from the plastic scintillators and the CsI detectors. An example of such an identification matrix is given in Fig. 6(a). It was obtained for the 10 – 11 degrees angular range, with a CH_2 target. The small contribution of the deuterons which reached the CsI detectors, and a part of the background, were rejected by applying two-dimensional contours around the proton band. Another source of background which is present in the proton band, was due to protons from nuclear reactions that occurred inside other multitarget box elements, different from the targets of interest. Mainly, they were protons arising from np scattering reactions in the cathode foils. That additional pollution had to be rejected with another technique which consisted of recording "blank-target" events with the MTGT emptied of targets. Subtraction of the corresponding spectra to those recorded during "physics" runs, was performed after normalization to the same neutron fluency and to the same data acquisition dead time. Examples of proton spectra associated to blank-target runs and physics runs are shown in Fig. 6(b).

With the CH_2 target, the energy calibration of the CsI detectors was done using protons produced in $\text{H}(n,p)$ reactions, for which the emission energies could be accurately calculated. In order to reject the contribution from $^{12}\text{C}(n,p)$ reactions, a pure carbon target was mounted together with the CH_2 target inside the MTGT. Data on both targets were recorded simultaneously, so that, after normalization to the same number of carbon nuclei as in the CH_2 target, events associated to $^{12}\text{C}(n,p)$ reactions could be subtracted from the spectrum obtained with the CH_2 target. Examples of spectra obtained with both targets are shown in Fig. 7, together with the proton spectrum resulting from the subtraction. The latter presents a peak and a tail, reflecting the incident neutron spectrum presented in Fig. 2. Both features correspond to $\text{H}(n,p)$ events induced, respectively, by 96 MeV projectiles and by neutrons of lower energies contained in the beam tail. The proton energy spectra were obtained after calibration of the CsI detectors and corrections for energy losses inside the set-up. These corrections were determined by Monte Carlo simulations for which attention has been paid to reproduce accurately the experimental conditions. The proton energy threshold equals 30 MeV. This large value is related to the long flight (about 84 cm) through of air and detector materials of the system.

B. Low-energy neutron rejection

In order to select only events induced by 96 MeV neutrons, the contribution of low energy neutrons had to be rejected. This has been done using a technique based on time-of-flight (tof). The tof measured were the sum of

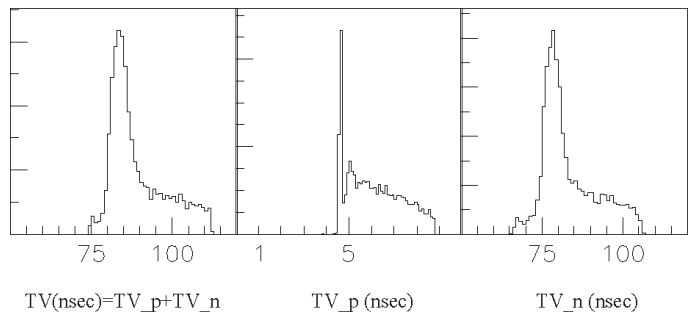


FIG. 8: Experimental determination of incident neutron time-of-flight.

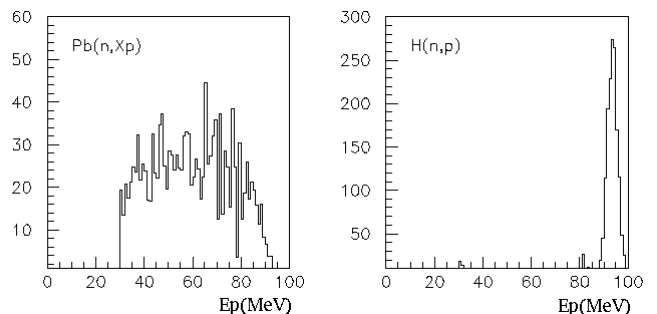


FIG. 9: Energy spectra of protons emitted in the angular range 10 – 11 degrees from neutron-induced reactions on a lead target (left part) and from the elastic scattering reaction (right part) at 96 MeV incident energy.

the neutron tof and the produced proton tof. From the proton energy, the corresponding tof can be calculated and subtracted from the total tof measured. The result is the tof of the neutron which induced the reaction. In Fig. 8 are presented total time-of-flight, proton tof and neutron tof spectra. The events associated to 96 MeV projectiles populate the peak centered at 78 nsec in the neutron tof spectrum. This time corresponds to the experimental path of 1062.8 cm. A selection of that peak could then be easily applied.

In this way, spectra of protons from reactions induced by 96 MeV neutrons were constructed. In Fig. 9 two examples of such spectra obtained for $\text{Pb}(n,Xp)$ and $\text{H}(n,p)$ reactions recorded simultaneously with the MTGT system are presented. As it can be seen, for $\text{H}(n,p)$ elastic scattering reactions, after selection, only the peak at high energy remains in the spectrum, compared to that of Fig. 7, while the contribution originating from low-energy neutrons has been completely removed. This is a confidence check of the time-of-flight method used for the event selection. The statistics accumulated in both spectra presented in Fig. 9 corresponds to about 2 hours of acquisition time.

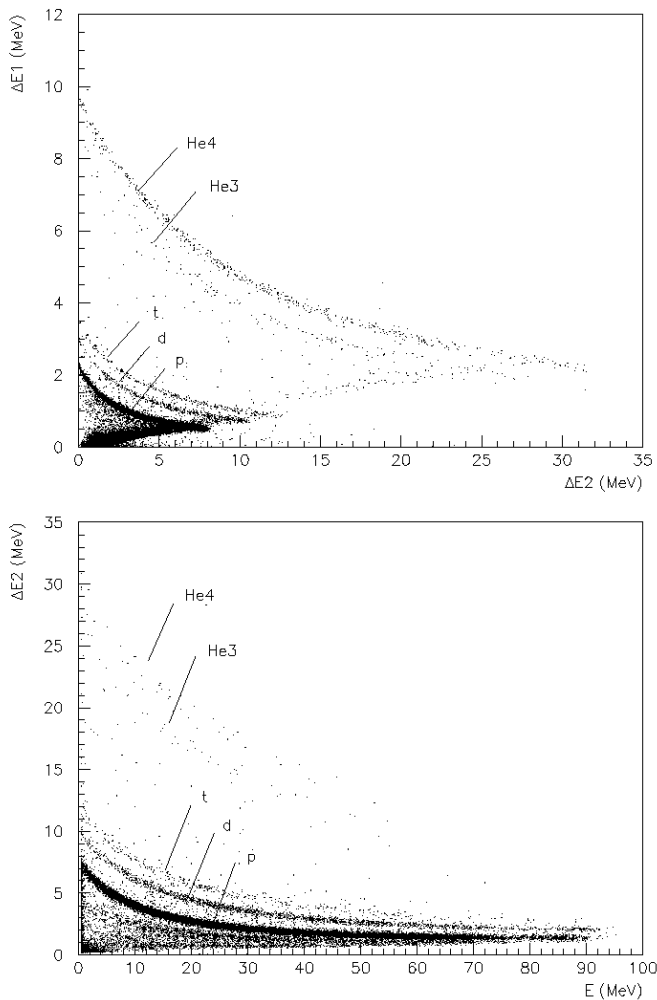


FIG. 10: Two-dimensional plots showing particles stopping in the second silicon detector (top) and in the CsI detector (bottom) of the telescope placed at 40 degrees using a CH_2 target.

C. Event sorting for MEDLEY set-up

For the MEDLEY set-up, the particle identification has been done using the well known ΔE - ΔE and ΔE - E techniques. Examples of two-dimensional plots obtained after energy calibration of each detector, for each particle type, are presented in Fig. 10. The top figure represents particles stopped inside the second silicon detector, while the lower one shows particles which reached the CsI scintillator.

For calibration purposes, the points where each particle type start to punch through the silicon detectors were used. The corresponding energies were calculated with the detector thickness given by the manufacturer and the stopping power data from Ref. [11]. In addition, for the thin silicon detectors, the calibration was checked using 5.48 MeV alpha particles which stopped inside these detectors and which were emitted by a ^{241}Am source. The

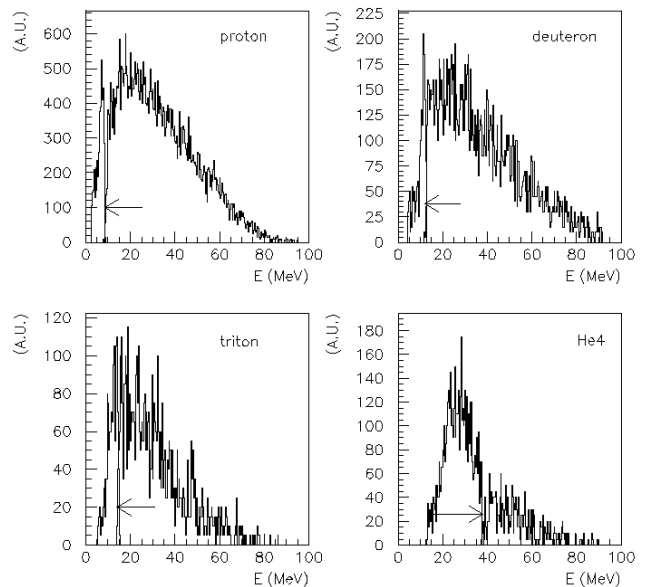


FIG. 11: Energy spectra for particles detected by the telescope placed at 40 degrees with all neutrons from the beam incident on a lead target.

energy deposited in the CsI(Tl) detectors has been further calculated for each particle type using the energy losses inside the silicon detectors. Supplementary calibration points in the case of protons were provided by the $\text{H}(n,p)$ reactions on a CH_2 target. The method and the different parameterizations used are presented in detail in Ref. [8].

Finally, the total energy of each emitted particle is deduced by adding the different energies deposited inside the three individual detectors of each telescope. Fig. 11 shows energy spectra of p, d, t and alpha particles obtained from a lead target with the telescope placed at 40 degrees. The arrows show the overlapping region between the second silicon and the CsI detector contributions.

The detection thresholds are given by the thickness of the first silicon detector. It is about 2 – 3 MeV for the hydrogen isotopes and about 9 MeV for the helium isotopes, as it can be seen in Fig. 10. The spectra had to be further corrected for the particle energy loss inside the emission target. Those corrections were calculated using Monte Carlo simulations, with targets of about 50 μm thickness. The maximum correction value estimated is less than 4 MeV, for low-energy alpha particles. This shows that the corrections to be applied remain within reasonable limits.

The rejection of events associated to low-energy neutrons was done with the same procedure as for SCANDAL (subsection B). The background is dominated by protons arising from neutron-induced reactions inside the beam tube, at the entrance of the vacuum chamber. That contribution is subtracted by using the spectra accumu-

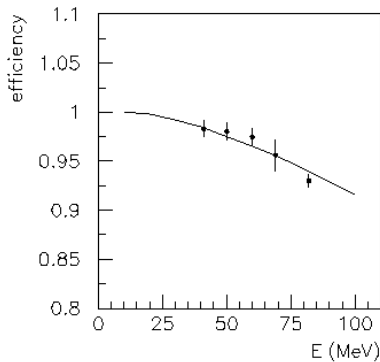


FIG. 12: Energy dependence of the CsI detection efficiency for protons. Simulation result (continuous line) is compared with the experimental values from Ref. [9].

lated during blank-target runs, applying a normalization to the same neutron fluency as for target-in runs, and taking into account corrections for the data acquisition dead time differences.

For the MEDLEY and SCANDAL set-ups, the CsI scintillator efficiency depends on the energy and type of the detected particle. Small corrections for the loss of light in the CsI detectors have then also to be applied. This effect is due to nuclear reactions which charged particles can undergo while slowing down inside the CsI. Corrections for this effect have been estimated for all charged particles, using reaction cross sections available in the GEANT library from CERNLIB [12]. Those estimations enable to determine the CsI detector efficiency as presented in Fig. 12 for protons (continuous line). The loss of light inside the CsI detector is rather important for high energy protons and it is less pronounced for heavier particles. The detection efficiency at 100 MeV equals 91% for protons, 93% for deuterons, 95% for tritons and 99% for alpha particles and it increases as the energy decreases. As shown in the figure, simulation results are in very good agreement with the experimental values from reference [9].

D. Cross section normalization

Due to the difficulty encountered when monitoring a neutron beam intensity, the absolute cross section normalization in neutron induced reactions is a notorious problem. In particular for our experiments, the uncertainty affecting the value given by the fission monitor equals 10 %, which induces large uncertainties for the values of the measured cross sections. Therefore, the cross sections are measured relatively to another one, considered as a reference. The reference cross section the most often used is the H(n,p) cross section, for which a recent measurement claims an absolute uncertainty of 2 % [13]. We have used the values given in that reference

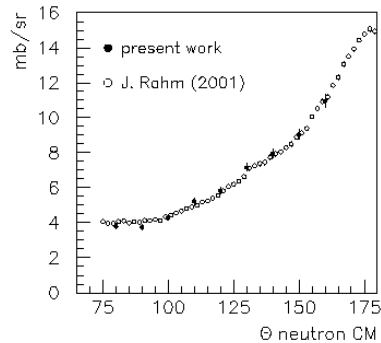


FIG. 13: Differential np scattering cross section at 96 MeV. The results obtained in the present work using SCANDAL set-up are compared to the data from reference [13].

to calculate the absolute cross sections. Nevertheless, in order to be able to apply the normalisation procedure, we have to measure in the same experimental conditions the number of protons emitted in H(n,p) reactions because that number intervenes in the normalisation factor. When measuring that number, we took the opportunity to remeasure the angular distribution of the H(n,p) cross section.

For that purpose, we used the SCANDAL set-up. We determined the number of recoiling protons after subtraction of the $^{12}\text{C}(n,p)$ reaction component and the background contribution, following the procedure presented in subsection A. The angular range being limited in our measurements to 80 – 160 degrees for neutrons in the center of mass system, we extracted values for the other angles by fitting our data with a fourth order Legendre polynomial. Then, considering other channels negligible at 96 MeV, we normalized the value of the deduced total np cross section to that given in Ref. [14]. Finally, we obtained the angular distribution which is presented in Fig. 13 together with the experimental results of Ref. [13]. We observe a very good agreement between both. However, the uncertainties of the cross sections from [13] are significantly smaller than in our experiment (2 %). Indeed, for our data, the statistical errors are typically in the range 1.5 – 2.8 %, and the total uncertainty is estimated of the order of 4.1 %, including the 1 % contribution from the total np cross section [14]. The systematical errors affecting our results arise from the subtraction of reactions on carbon, from the integration over the np peak and from the rejection of events induced by low-energy neutrons.

For the SCANDAL set-up, the MTGT system was used to measure at the same time protons emitted from the target under study (iron, lead or uranium) and in H(n,p) reaction from the CH_2 target. The normalisation procedure could then be applied without precise knowledge of the neutron flux. For the MEDLEY set-up, all data have been normalized using the H(n,p) scattering peak recorded by the telescope placed at 20 degrees during separate runs with a CH_2 target.

For the proton emission, data recorded using the SCANDAL and MEDLEY set-ups were individually normalized, allowing two independent determinations of the cross sections for all targets studied. With this procedure, the estimated systematical uncertainties of the experimental cross sections are not greater than 5.1 %. To calculate this value, we took into account the contributions from the number of target nuclei (2 %), the solid angles calculated by simulations (0.75 %), the beam monitor stability during the data taking (2 %), the number of recoiling protons from the np reaction (3.7 %) and the reference np cross sections (2 %) according to [13].

IV. EXPERIMENTAL RESULTS

The double-differential cross sections of light charged particles were measured for three targets, Fe, Pb, U, with natural isotopic compositions, over an angular range of 20 – 160 degrees. For the MEDLEY set-up, the low energy threshold was 4 MeV for hydrogen isotopes, 12 MeV for ^3He and 8 MeV for alpha particles. For the SCANDAL set-up, it was 35 MeV for protons. Due to the detector energy resolution and the available accumulated statistics, a 4 MeV bin size has been chosen for the energy spectra.

In the left part of Fig. 14, proton double differential cross sections measured independently with the MEDLEY set-up (full circles) and with the SCANDAL set-up (open circles) are compared. The spectra correspond to the Fe target and a 20 degrees emission angle. Over the energy range covered by both detection devices, we observe a very good agreement. This shows that the systematical uncertainties induced by the cross section normalization are small. We obtained similar results for the other targets (Pb and U) and over the full angular range. In addition, it shows that the limited angular resolution of MEDLEY does not distort the distributions which are comparable to that obtained with SCANDAL, for which the angular resolution is much better. The right part of Fig. 14 gives a comparison of the $\text{Fe}(n,\text{Xp})$ cross section measured at 20 degrees with MEDLEY, with the data from Ref. [15] which were obtained using the magnetic spectrometer LISA. A very good agreement is found also between these two measurements. This shows the quality of our measurements and of the data analysis procedures employed. We observed a similar agreement for the $\text{Pb}(n,\text{Xp})$ cross sections.

In Fig. 15 are presented experimental double-differential cross sections for p, d, t (top, middle, bottom lines respectively) produced in 96 MeV neutron induced reactions on Fe, Pb and U targets (left, middle and right rows respectively) and measured with the MEDLEY set-up. In Fig. 16, for the same reactions, we report the complementary production cross sections of ^3He and alpha particles (top and bottom figures respectively). The errors shown are purely statistical.

The general trend observed is a decreasing emission

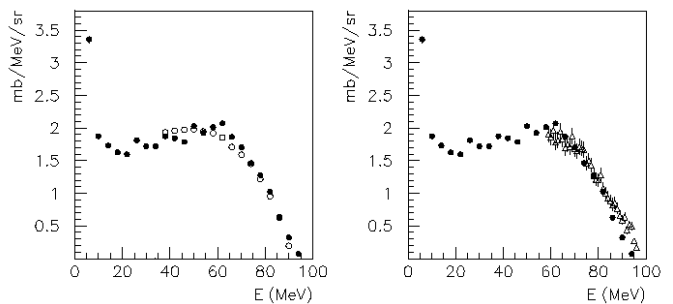


FIG. 14: Left panel: $\text{Fe}(n,\text{Xp})$ double-differential cross sections measured with MEDLEY set-up at $\theta=20$ degrees (full circles), compared to the SCANDAL results (open circles). Right panel: same data compared to those from Ref. [15] (open triangles).

probability with increasing angle, over the full energy range. The angular distributions are slightly forward peaked at low energies, and at backward angles, the emission probabilities are very low for energetic particles. In the case of the iron target, a quasi-isotropic component is observed at very low energy (0 – 10 MeV). This contribution is not present for heavier targets, for which Coulomb effects are much larger. For the rest of the energy range, the distributions obtained with the three targets are very similar in shape. For ^3He particles, distributions have been measured only for the iron target. Despite the long data acquisition time, no corresponding events were recorded for the other targets. This is related to the very low ^3He emission probability for heavy targets which has been already observed in Ref. [17], where the ^3He production rate in 63 MeV proton induced reactions on ^{208}Pb is about 10 times smaller than for tritons.

For a more detailed analysis of the particle emission mechanisms, a separate inspection of angular and energy differential distributions is needed. The angular distributions were obtained from double-differential cross sections by integration over the full energy range. For the energy distributions, we used the Kalbach systematics [16] in order to extrapolate the experimentally available angular range over the entire space. Finally, the total production cross sections were derived for each particle type by integrating the corresponding energy-differential cross sections over the experimental energy range.

The energy-differential cross sections are presented in Fig. 17 for the iron and lead targets. The results obtained with the uranium target are very similar to those extracted for the lead one. By analyzing the spectra, we distinguish two regions. For energies greater than about 20 MeV, proton and deuteron spectra are very similar in shape, the emission probability decreasing slowly with energy for both targets. In the case of the iron target, the triton and ^3He spectra also show a similar behavior. For alpha particles, the spectra decrease very rapidly with energy. For a given particle, the shapes of the iron and

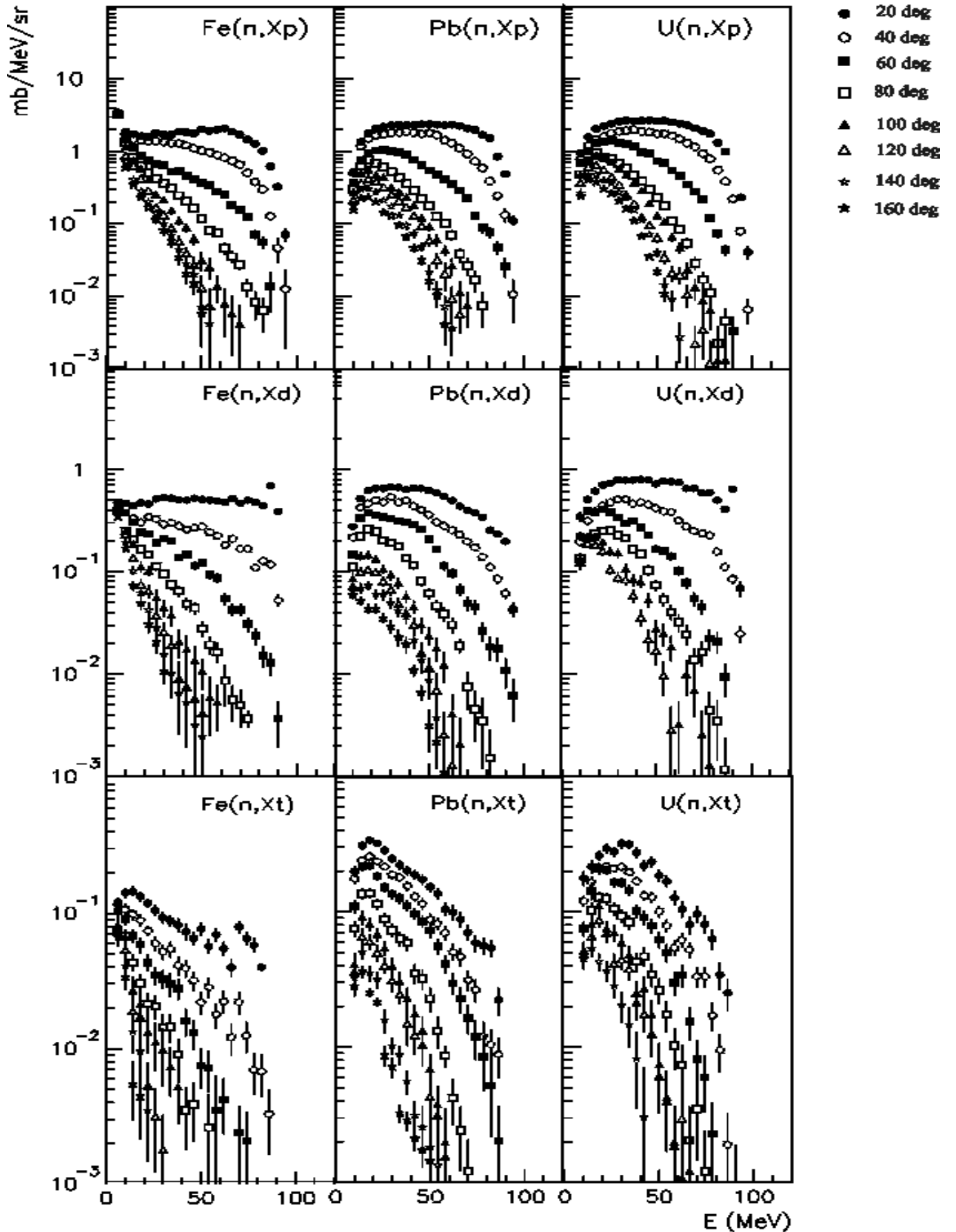


FIG. 15: Double-differential cross sections for p, d, t particles (top, middle and bottom lines respectively) emitted in 96 MeV neutron-induced reactions on Fe, Pb and U targets (left, middle, right rows respectively).

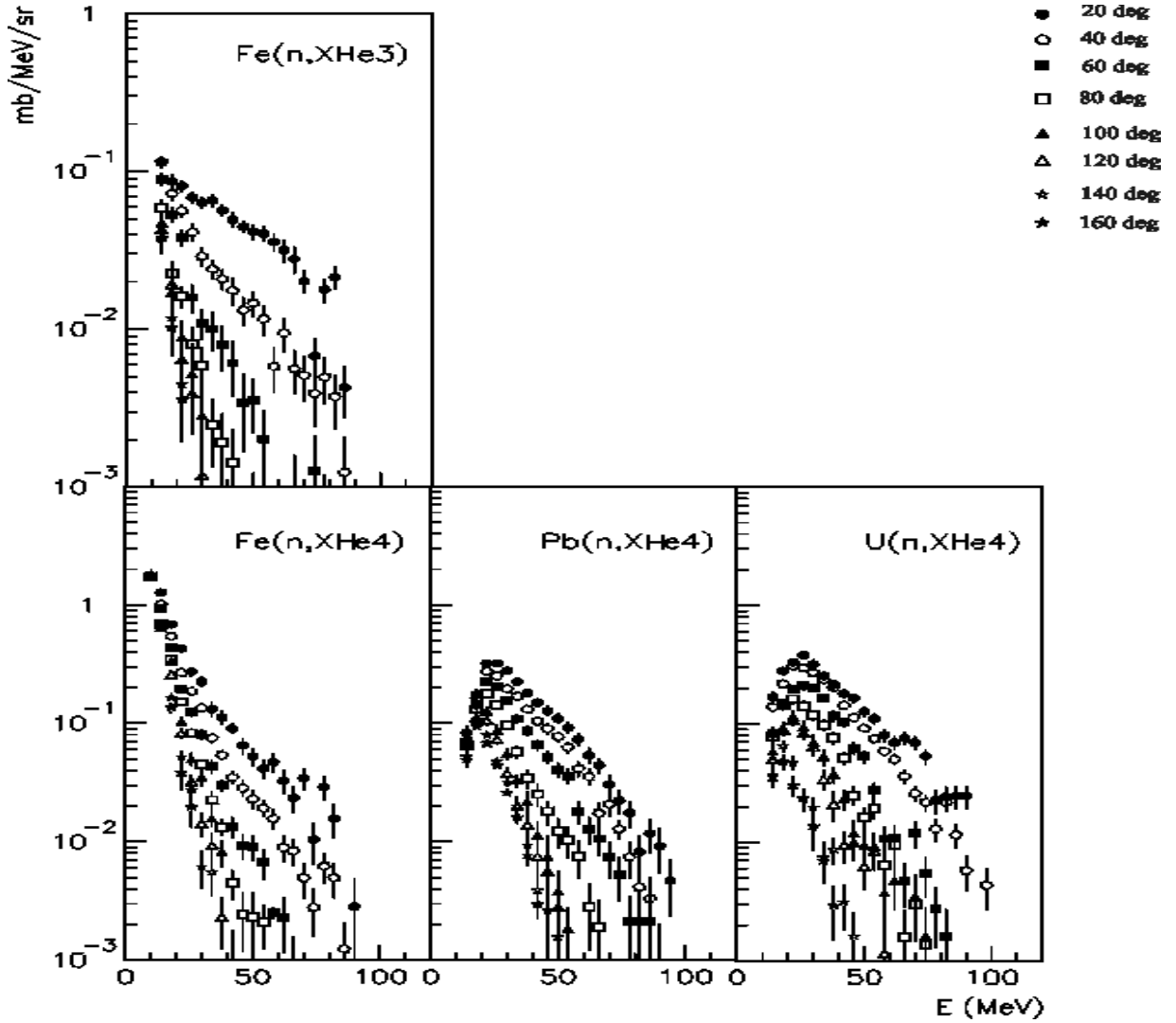


FIG. 16: Same as Fig. 15 for helium isotopes.

lead distributions are very similar. In this energy region, the emission probability distributions have steeper slopes for heavy particles than for light ones. Another important aspect to be noticed is the decreasing emission probability with the nucleon number of the emitted particle. However, an exception is observed for alpha particles for which the production cross sections in the low-energy part of the continuum region ($20 \text{ MeV} < E < 35 \text{ MeV}$) are larger than for tritons, suggesting a more complex mechanism for their emission. For low emission energies ($E < 20 \text{ MeV}$), a dominant contribution is observed for all particles in the case of the iron target. The shape of the distributions in Fig. 17, correlated to the slow variation of the amplitude with the emission angle observed in Figs. 15 and 16, suggests that these low energy particles are emitted mainly during the evaporation process of an excited nucleus. This component is not present in the spectra obtained with the lead and uranium targets

because, for heavy targets, the emission of low energy particles is strongly inhibited by Coulomb effects. This explains the low cross sections found in this energy range for both lead and uranium targets.

Fig. 18 shows the angular distributions obtained by integrating double-differential distributions. Due to the detection thresholds, the integration domains range over $4 - 96 \text{ MeV}$ for hydrogen isotopes, $12 - 96 \text{ MeV}$ for ^3He and $8 - 96 \text{ MeV}$ for alpha particles. For all particles, the distributions are strongly forward peaked, suggesting that non-equilibrium processes are dominant for the reactions under study. An exception can be noticed for alpha particles in $\text{Fe}(n,X)$ reactions, where the distribution is almost flat for angles larger than 50 degrees. This suggests that the emission of alpha particles in the backward hemisphere could result mainly from evaporation processes. For a given particle, the angular distributions are more forward peaked for the heavier nuclei, suggest-

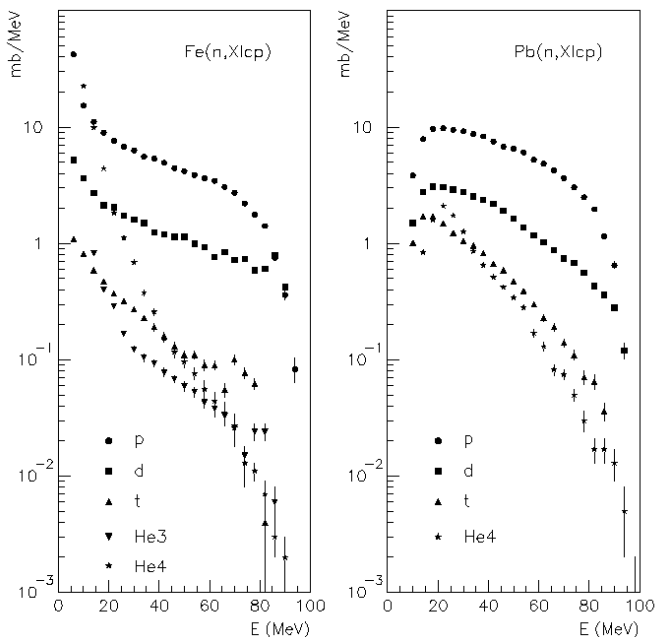


FIG. 17: Energy distributions for light charged particle produced in 96 MeV neutron induced reaction on iron and lead targets (left and right panels respectively).

ing that the non-equilibrium component increases with the nucleon number of the target.

This can also be observed from Table I, where integrated total cross sections (second column) and integrated non-equilibrium cross sections (third column) are presented as a function of the target mass, for all particles. Depending on the system considered, the non-equilibrium cross sections were extracted with different methods. For the $\text{Fe}(n,\text{Xlcp})$ reactions (lcp refers to light charged particles), the low-energy contribution in the energy-differential cross sections (Fig. 17) was fitted with an exponential function and its integral was then subtracted from the total cross section for each particle. For lead and uranium targets, we made the assumption that all particles were emitted during non-equilibrium processes, i.e., in a first approximation, the rather small contribution of evaporated particles expected at low energy is neglected.

The values from Table I show that for all targets studied, more than 30% of the total light charged particle production are particles heavier than protons. This is an important aspect to be pointed out, because, with such a production rate, the contribution of these particles should not be neglected.

V. THEORETICAL CALCULATIONS

At this moment, the exciton model [2] is the most commonly used to calculate the pre-equilibrium emission in

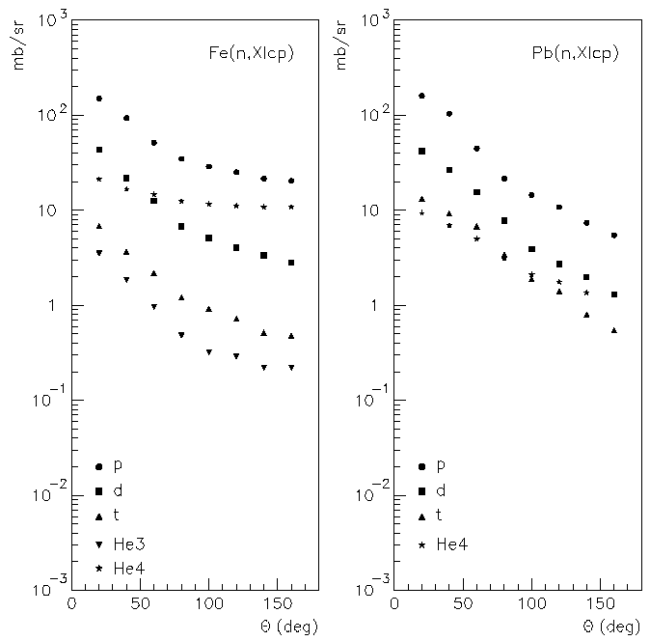


FIG. 18: Angular distributions for light charged particle produced in 96 MeV neutron induced reaction on iron and lead targets (left and right panels respectively).

nucleon-induced reactions at intermediate energies. This model assumes that the excitation process takes place by successive nucleon-nucleon interactions inside the nucleus. Each interaction produces another exciton, leading the system to the final state of statistical equilibrium through more complex states. Occasionally a particle can receive enough energy to leave the system and subsequently be emitted. The resulting pre-equilibrium spectrum is the sum of the contribution from each state. Particles emitted in the early stages have more energy than those emitted in the later ones. In the framework of this model, only energy distributions of emitted particles can be calculated.

The GNASH code [6] is one example which uses the exciton model to calculate the pre-equilibrium component. It is able to calculate spectra for nucleons and complex particles. In this code, the equilibrium contribution is calculated using the Hauser-Feshbach formalism [32]. Cross sections which were evaluated with GNASH are at present implemented in MCNPX, a code widely used for specific applications such as medical or engineering studies. In Figs. 19 and 20, we compare, respectively, the $^{56}\text{Fe}(n,\text{Xlcp})$ and $^{208}\text{Pb}(n,\text{Xlcp})$ energy-differential cross sections of the present work (points), to the GNASH predictions (histograms) obtained with MCNPX. The maximum value in the alpha particle spectrum for the iron target has been set to 1 mb/MeV for a better visualisation. While the proton emission is relatively well described, we observe that the production of complex particles is strongly underestimated.

This comparison suggests that significant improve-

| Reaction | Total cross section (mb) | Non-equilibrium cross section (mb) |
|-------------------------|-----------------------------|---------------------------------------|
| Fe(n,Xp) | 584±29.2 | 326 |
| Pb(n,Xp) | 485±24.3 | 485 |
| U(n,Xp) | 589±29.5 | 589 |
| Fe(n,Xd) | 131±6.5 | 96 |
| Pb(n,Xd) | 137±6.9 | 137 |
| U(n,Xd) | 170±8.5 | 170 |
| Fe(n,Xt) | 21±1.1 | 15 |
| Pb(n,Xt) | 53±2.7 | 53 |
| U(n,Xt) | 54±2.8 | 54 |
| Fe(n,X ³ He) | 10±0.5 | 7 |
| Fe(n,X ⁴ He) | 167±8.3 | 31 |
| Pb(n,X ⁴ He) | 45±2.2 | 45 |
| U(n,X ⁴ He) | 52±2.6 | 52 |

TABLE I: Total light charged particle integral cross sections and estimated contributions from the non-equilibrium emission in neutron induced reactions at 96 MeV.

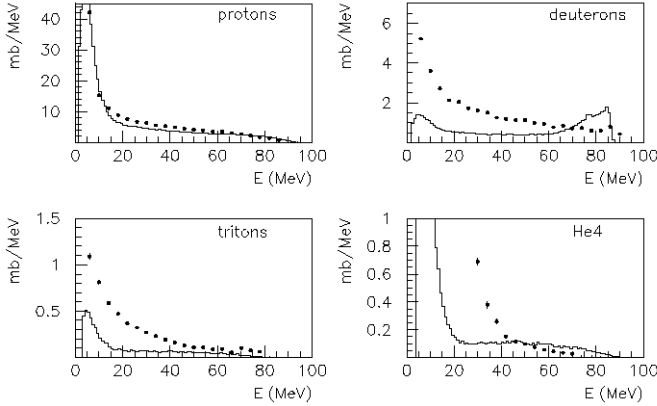


FIG. 19: Energy-differential cross sections calculated using the GNASH code for the $^{56}\text{Fe}(n,Xlcp)$ reaction at 96 MeV (histograms) compared with the present experimental results (points).

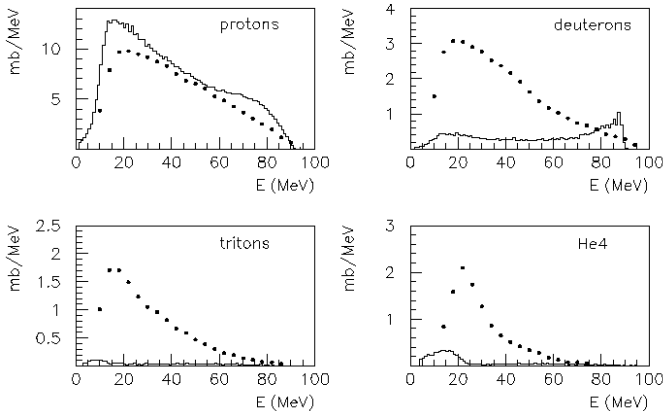


FIG. 20: Same as in Fig. 19 for the $^{208}\text{Pb}(n,Xlcp)$ reaction.

ments are needed in the original exciton model in order to increase its prediction level concerning the cluster emission. To modify it according to this request, a first approach was proposed in 1973 by Ribanský and Obložinský [3]. It introduces the probability of a cluster formation during the nucleon-nucleon interactions inside the target. In 1977, Kalbach formulated a second approach [4] which includes contributions from direct pick-up and knock-out mechanisms. Both approaches have been tested in the past against data and they lead to a satisfactory agreement with the experimental results [4, 5], despite their completely different basic assumptions. Nevertheless, conclusions about their global predictive power were limited, mainly because a restricted number of experimental results were available at that moment. In order to get a wider view on their predictive capabilities, we performed calculations with both approaches for the $^{56}\text{Fe}(n,Xlcp)$, $^{208}\text{Pb}(n,Xlcp)$, $^{238}\text{U}(n,Xlcp)$ reactions at 96 MeV, but also for other projectiles, at different incident energies and for other targets, for which experimental data are available in the literature. In the forthcoming subsections, we will give a basic description of both approaches and discuss the comparisons of the calculations with a set of data that cover a wide domain of reaction entrance-channel parameters.

A. Cluster formation probability in nucleon-nucleus reactions

Due to the difficulties encountered by the original exciton model proposed by Griffin to reproduce the experimental distributions of complex particles, it has first been modified by Ribanský and Obložinský [3]. The modification consists of the introduction in the particle production rate expression of a multiplicative term containing the cluster formation probability γ_β where β is the type of the emitted particle. The physical meaning of this

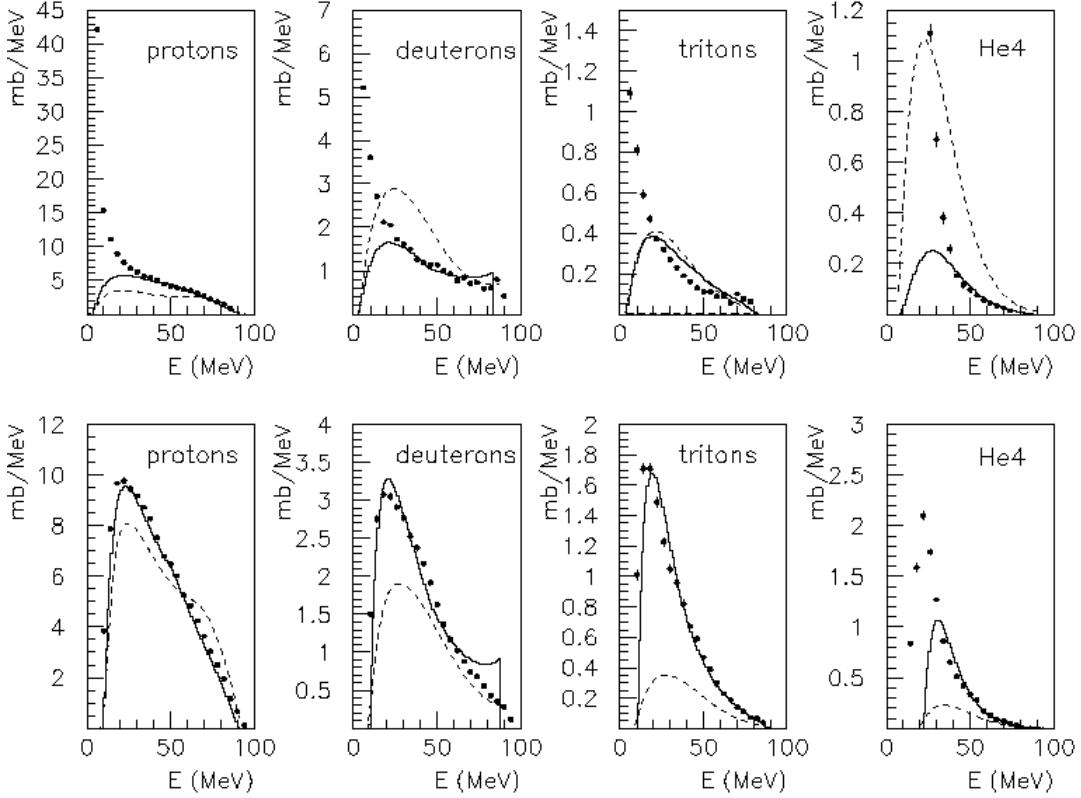


FIG. 21: Energy-differential cross sections calculated using PREEQ (histograms) and PRECO-2000 (dashed lines) for $^{56}\text{Fe}(n,Xlcp)$ (top) and $^{208}\text{Pb}(n,Xlcp)$ (bottom) reactions at 96 MeV, compared with the experimental results of the present work (points). Maximum value in the alpha-particle spectrum in the case of the iron target has been set to 1.2 mb/MeV for a better comparison.

parameter has been given in Ref. [18] in the framework of the coalescence model. This approach assumes that complex particles are formed during the pre-equilibrium stage from excited nucleons which share the same volume in the momentum space. In this way, for example, an excited proton and an excited neutron can coalesce into a deuteron if the transverse momentum between both is small. The drawback of this approach is its limited predictive power since the parameter γ_β has to be adjusted in order to reproduce as well as possible the amplitude of the experimental energy-differential distribution under study. Nevertheless, it is always interesting to compare the tuned results of a model with experimental data.

The formation probability γ_β of a complex particle β is given as a function of the radius of the coalescence sphere P_0 in the momentum space by the formula:

$$\gamma_\beta = \left| \frac{4}{3}\pi(P_0/mc)^3 \right|^{p_\beta-1} \quad (1)$$

where p_β is the number of nucleons of the emitted particle. Of course, $\gamma_\beta=1$ in the case of the emission of a nucleon. According to equation (1), γ_β and thus, P_0 is the free parameter of the model.

The following expression for the cluster formation

probability has been proposed in the Ref. [19]:

$$\gamma_\beta = (p_\beta)^3 (p_\beta/A)^{p_\beta-1} \quad (2)$$

where A is the mass of the target nucleus. This approach is implemented in the latest version of the code GEANT [21], which is intensively used for simulations among the physics community. However, calculations from Ref. [19] strongly overestimates deuteron, triton and ^3He distributions, while the production rates for alpha particles are underestimated. This shows that the calculation of the cluster formation probability according to equation (2) is not very appropriate. For this reason, calculations in this work have been done with the PREEQ program [20], keeping the cluster formation probability as a free parameter. A complete explanation about the different parameters of the model and the method we applied to calculate them can be found in Ref. [5]. In the forthcoming discussion, we will focus onto the cluster formation probability γ_β because of its particular importance for the model predictions.

In the first step of our investigation, we performed calculations with PREEQ for the 96 MeV neutron induced reactions presented in this work. We determined two sets of values for the γ_β parameter by normalizing

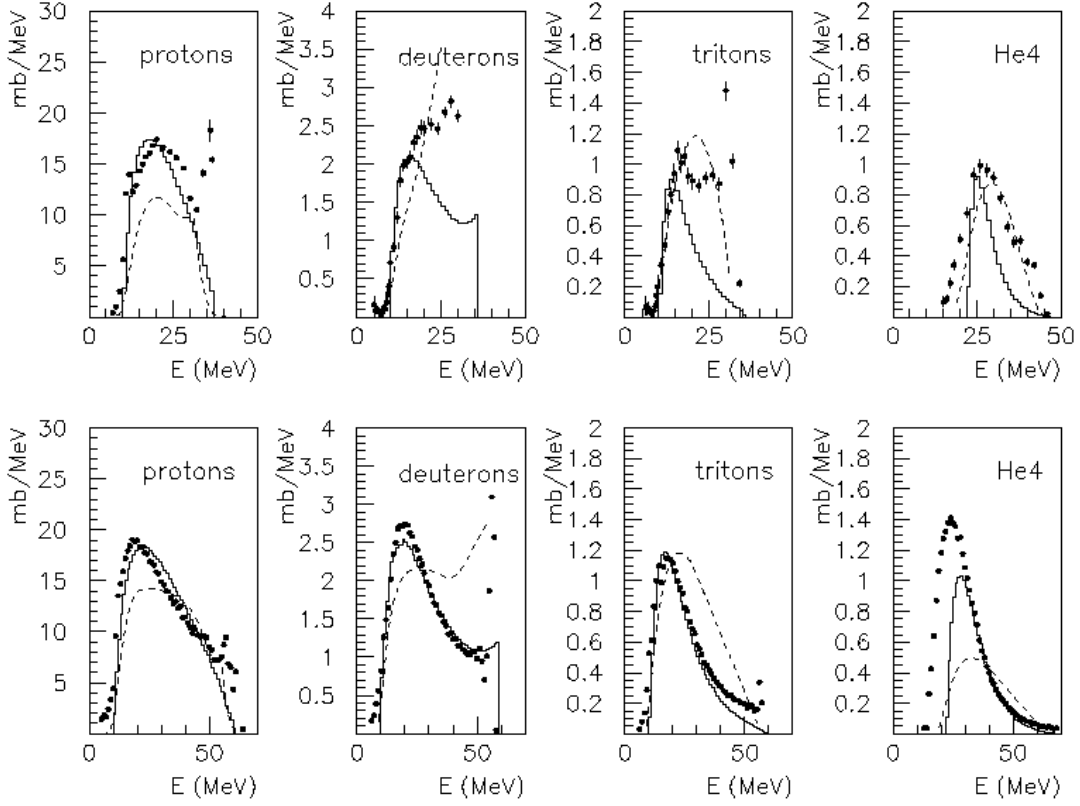


FIG. 22: Energy-differential cross sections calculated using PREEQ (histograms) and PRECO-2000 (dashed lines) for $^{209}\text{Bi}(p,Xlcp)$ reactions at 39 MeV (top) and $^{208}\text{Pb}(p,Xlcp)$ reactions at 63 MeV (bottom), compared with the experimental results from Ref. [22] and [17] (points).

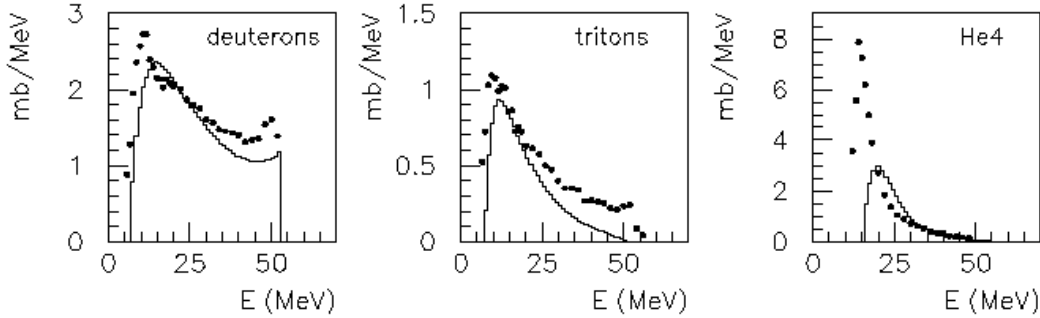


FIG. 23: Energy-differential cross sections calculated using the PREEQ code (histograms) for $^{120}\text{Sn}(p,Xlcp)$ reaction at 62 MeV compared with the experimental results from the Ref. [22] (points).

individually the calculated energy distributions to the $\text{Fe}(n,X)$ and $\text{Pb}(n,X)$ experimental data. For those reactions, PREEQ results (histograms) and data (points) are presented in Fig. 21 for ^{56}Fe and ^{208}Pb targets. We have to remind that the model calculates only the pre-equilibrium component of the emission spectra, so that in our comparison, we should not consider neither the low-energy region populated with particles evaporated by excited nuclei, nor the high-energy region where di-

rect reactions are supposed to be dominant. Considering those restrictions, we observe that the shapes of the calculated distributions are in good agreement with the experimental results. As expected, the model fails in reproducing the very low-energy component of the iron spectra. For all particles in the $^{208}\text{Pb}(n,X)$ reactions, except alpha particles, the calculated pre-equilibrium contribution accounts for almost the entire energy range, showing that almost all particles are emitted during

the pre-equilibrium stage. For alpha particles, the pre-equilibrium processes are still underestimated by PREEQ in the low-energy region of the continuum. By comparison with the GNASH predictions presented in Figs. 19 and 20, we clearly see that this approach improves dramatically the original exciton model, for all particles.

For protons, for which the γ_β parameter equals 1 and has not to be adjusted, the amplitudes of the distributions are very well described by the model in the energy range where it is applicable. It must be pointed out that only the primary pre-equilibrium contribution is calculated by this code. The good agreement found for protons suggests that the second-chance preequilibrium component is very small, in agreement with the calculations from Ref. [23]. For complex particles, no conclusion about the predictive capabilities of PREEQ can be drawn at the moment, the amplitude of the distributions being obtained by adjusting the γ_β parameter in order to get a good agreement with the experimental data. Therefore, the next step in our analysis was to check the stability of this parameter while changing the entrance channel, i.e., the incident energy and the projectile, for a target nucleus in the mass region $A = 208$. For that aim, using the values of the cluster formation probabilities previously obtained for the 96 MeV $^{208}\text{Pb}(n,X)$ reactions, we calculated the energy differential cross sections for 39 MeV $^{209}\text{Bi}(p,X)$ and 63 MeV $^{208}\text{Pb}(p,X)$ reactions. In Fig. 22, the resulting PREEQ calculations (histograms) are compared with the experimental data (points) measured at 39 MeV with a ^{209}Bi target [22] (top panels) and to the data measured at 63 MeV with the ^{208}Pb target [17] (bottom panels). Over the energy domain where the model is applicable, we observe again a good agreement between the calculations and the experimental results. In addition and especially at 39 MeV, we see that the non-calculated direct process contribution is dominant.

From this study, we conclude that the free parameter γ_β depends neither on the projectile type (neutron or proton) nor on the incident energy and that, once the cluster formation probability has been adjusted on reaction system, the model has a good predictive power for reactions with the same target. To go further, we have now to investigate its possible dependence with the target mass. Since we have just determined the formation probability γ_β for two target nuclei with masses $A = 56$ and $A = 208$, we choose an intermediate target with a mass $A = 120$ for which experimental data were measured, i.e., the $^{120}\text{Sn}(p,Xlcp)$ reaction at 62 MeV incident energy [22]. With the same method described previously, we calculated the new set of γ_β values associated to the ^{120}Sn target. In Fig. 23, we compare the corresponding PREEQ calculations (histograms) to the data (points). As for the other targets, we observe the same global good reproduction of the data in the pre-equilibrium energy region.

In Table II, we gather the values of the cluster formation probabilities, as well as the related P_0 parameters, obtained for the three target nuclei $A = 56$, $A = 120$ and

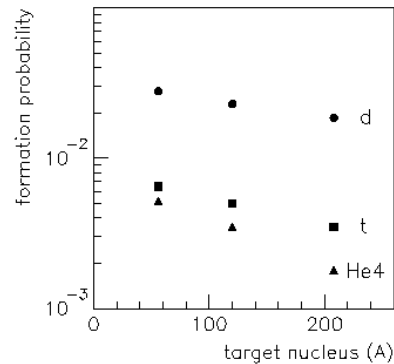


FIG. 24: Formation probability for each complex particle versus target mass.

$A = 208$ and for each complex particle type. The formation probability for each particle type is also represented as a function of the target mass in Fig. 24.

We observe that for a given particle, the formation probability and then the coalescence sphere radii, is smaller for heavier nuclei. Under the assumption of phase space relations, a smaller P_0 value means a larger volume inside the nucleus from which the particle is emitted. This volume is then larger for heavier nuclei. In addition, for a given target nucleus, the figure shows that the formation probability decreases as the number of nucleons of the emitted particle increases. This could be explained by the fact that it is less probable, for example, for three nucleons to coalesce in order to form a triton, than for two nucleons to form a deuteron. The formation probability of deuterons is much larger than for other complex particles, suggesting that the most probable mechanism is the pick-up of one nucleon by another.

The presently obtained values are in rather strong disagreement with those from Ref. [19]. Thus, for the $^{208}\text{Pb}(p,Xlcp)$ reaction, the γ_β probability calculated according to equation (2) is 0.077 for deuterons, 0.0056 for tritons and 0.00046 for alpha particles. As it can be observed, the values for hydrogen isotopes are larger than those obtained in this work, leading to the overestimation found in the Ref. [19] for the production of these particles. On the other hand, the values for alpha particles are smaller than ours and thus the distributions calculated in Ref. [19] are systematically below the experimental results.

Another interesting aspect to point out is that the presented P_0 values obtained for nucleon-nucleus reactions are in the same range as those extracted for reactions induced by complex projectiles (deuterons, ^3He and alpha particles) at intermediate energies [24] and for reactions induced by heavy ions at high energies [25, 26]. This suggest a weak dependence of this parameter with the projectile mass and energy.

To conclude, compared to the original exciton model existing in the GNASH code, the approach proposed

| Target | Emitted particle | Formation probability γ_β | P_0 (MeV/c) |
|-------------------|------------------|--------------------------------------|------------------|
| ^{56}Fe | d | 0.0278 | 175 |
| | t | 0.0065 | 250 |
| | ^3He | 0.0060 | 246 |
| | ^4He | 0.0052 | 322 |
| ^{120}Sn | d | 0.0230 | 164 |
| | t | 0.0050 | 238 |
| | ^4He | 0.0035 | 304 |
| ^{208}Pb | d | 0.0186 | 153 |
| | t | 0.0035 | 225 |
| | ^4He | 0.0018 | 286 |

TABLE II: Cluster formation probability in nucleon-induced reactions on three targets and corresponding radii of the coalescence sphere in the momentum space.

by Ribanský and Obložinský's and implemented in the PREEQ code improves greatly the predictions concerning complex particle production rates in pre-equilibrium processes, with the adjustment of one free parameter depending only on the target mass.

B. Exciton model and direct reactions

In order to modify the original exciton model concerning the complex particle emission in nucleon-induced reactions, a completely different approach has been proposed by Kalbach [4]. It is based on the fact that direct reactions such as the nucleon pick-up process and the cluster knock-out process are not included inside the exciton model. Therefore this approach calculates their associated contributions separately and add them to the pre-equilibrium component calculated with the original exciton model. Contrarily to the PREEQ program, this approach does not use any multiplication factor in the particle production rate expression and thus, it has no adjustable parameter. In other words, this approach proposes to replace the cluster formation probability introduced in Ref. [3] by the contribution of direct reactions. This modification is taken into account in the code PRECO-2000 [27] which calculates nucleon and complex particle non-equilibrium spectra in nucleon-induced reactions using: i) the two-component version of the exciton model and ii) phenomenological models for direct reaction processes. This code is open to the community via the Data Bank Computer Program Services of NEA. The same approach has been recently implemented in the TALYS code [28], which is still under development and therefore not yet available to the community.

Calculations have been done with the PRECO-2000 code using the set of global parameters recommended by the author for the contribution of direct processes. Details can be found in Ref. [27]. For the exciton model contribution, the same values for specific parameter as for the PREEQ calculations have been used. In Fig. 25 an example of the PRECO-2000 results obtained for the

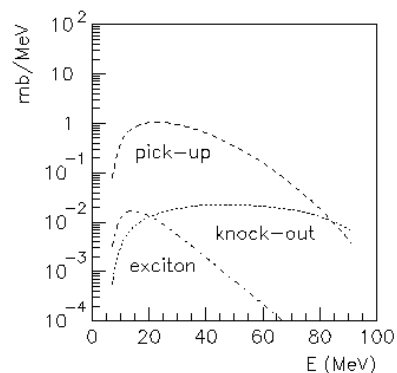


FIG. 25: Different mechanism contributions in the non-equilibrium alpha particle spectrum calculated using the PRECO-2000 code for the $^{56}\text{Fe}(n,X)$ reaction at 96 MeV.

alpha-particle emission in $^{56}\text{Fe}(n,X)$ reactions at 96 MeV is given. The three individual contributions in the non-equilibrium spectrum are displayed. We observe that the very low contribution of the pre-equilibrium processes predicted by the exciton model (dash-dotted line) is compensated by the other two direct processes now included, i.e, the pick-up of three nucleons (dashed line) and the knock-out of alpha particles (dotted line) which are assumed to be pre-formed inside the nucleus. The total non-equilibrium spectrum is obtained by summing all these contributions.

Following the same procedure as in the previous subsection, calculations have been performed first for the data that we measured at 96 MeV. The results are presented in Fig. 21 for the $^{56}\text{Fe}(n,Xlcp)$ and $^{208}\text{Pb}(n,Xlcp)$ reactions (dashed lines). The disagreement with the experimental distributions is rather strong for both systems. For the iron case, the non-equilibrium complex particle production is overestimated while the proton emission is underestimated. For the lead target, composite ejectile rates are underestimated, as well as the proton distribution. In addition, for a given target, the disagree-

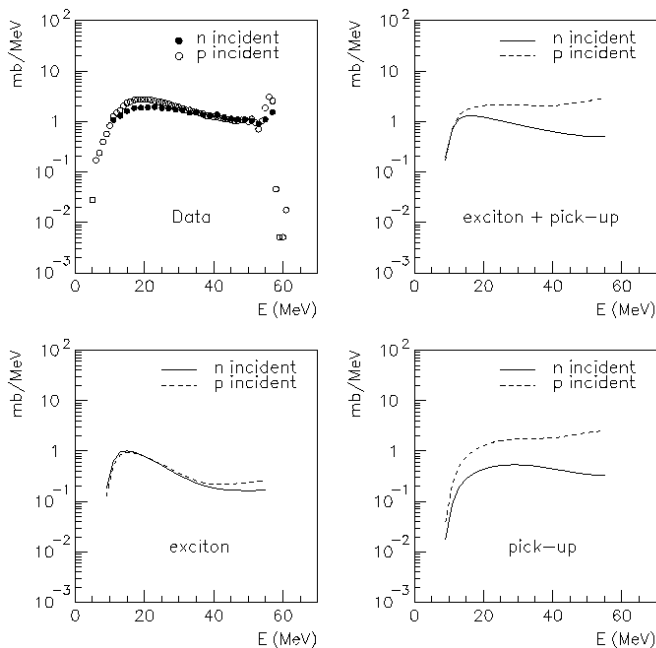


FIG. 26: Deuteron emission in proton and neutron induced reactions on ^{208}Pb at 63 MeV. Experimental results (top left panel) are compared to the distributions calculated using PRECO-2000 code (top right panel). Contributions from pre-equilibrium (exciton model) (left bottom panel) and nucleon pick-up reaction (bottom right panel) are presented.

ment seems to become more important as the mass of the emitted particle increases. Even if the model in PRECO-2000 code predicts more particles in the pre-equilibrium region than GNASH does, experimental shapes and amplitudes are not as well reproduced as with the PREEQ code. In the case of nucleon ejectiles, the secondary pre-equilibrium emission can be considered in this code. However, this contribution was not included in the calculated spectra in order to get the same calculation conditions as in the previous subsection. This can explain the underestimation found for energies around 20 MeV in the proton spectra.

Despite its bad data reproduction observed at 96 MeV, we tested PRECO-2000 again by changing the incident particle and energy of the entrance channel. Doing so, we found a better agreement as it can be seen in Fig. 22, where the predictions of the PRECO-2000 code (dashed lines) for the 39 MeV $^{209}\text{Bi}(p, Xlcp)$ (top panels) and the 63 MeV $^{208}\text{Pb}(p, Xlcp)$ (bottom panels) reactions are compared to the experimental results from the Refs. [22] and [17] (points). Even if a tremendous disagreement still exists at low incident energies, the model predictions are sensibly improved with proton projectiles compared to those related to incident neutrons at 96 MeV. This suggests that the PRECO-2000 predictions strongly depend on the incident energy and the projectile type. That latter aspect can be studied in more detail since data with both neutron and proton projectiles are available

for ^{208}Pb at the same incident energy (63 MeV). In Fig. 26, are presented the experimental energy distributions of deuterons for both reaction types (top left panel): i) (p,xd) [17] (open circles), and ii) (n,xd) [29] (full circles). The experimental results are very similar in shape and in amplitude for both projectiles. The corresponding PRECO-2000 calculated distributions are shown in the top right panel. As it can be seen, the theoretical distributions are very different when changing the incident nucleon type (neutron or proton), in a strong contradiction with the data. This disagreement does not originate from the pre-equilibrium contributions calculated by the exciton model because we checked that the corresponding distributions are similar for neutron and proton induced reactions (bottom left panel). On the other hand, the calculated contributions for the nucleon pick-up process (right bottom panel) are very different from each other and, since this mechanism is dominant, this difference generates the disagreement observed with the data. To conclude, the contribution of direct reactions like it is calculated in PRECO-2000 strongly depends on the incident particle type, contrary to the experimental data. This effect constitutes of course a shortcoming of the model.

C. Particle emission at equilibrium

Compared to PRECO-2000 simulations, the calculations performed with the code PREEQ have shown that this last approach allows a better description of the particle emission in the pre-equilibrium stage. For that reason, the results obtained with this model will be used in the further discussion.

As already commented in a previous section, the results presented in Figs. 21 and 22 suggest that for heavy targets, almost all particles are emitted during the pre-equilibrium phase of the reaction. Except for low-energy alpha particles, the PREEQ calculated distributions allow a good description of the experimental results over the full energy range, showing that the contribution of the evaporation process should be small. On the other hand, for light target nuclei (Figs. 21 and 23), the low-energy component of the experimental distributions suggest that the particle emission at equilibrium is rather important.

In this subsection, we propose to determine the contribution of the evaporation process. This component can be calculated separately assuming that it results from two different sources. The first source is the so-called "pure evaporation" and concerns the evaporation from the compound nucleus which has reached a statistical equilibrium. In Ref. [30], its contribution is given by a fraction $f_{EQ}(E) = (1 - f_{PE}(E))$ of the total reaction cross section, where $f_{PE}(E)$ is the fraction of the pre-equilibrium emission, considering n, p, d, t, ^3He and alpha particles, and E is the composite nucleus excitation energy. We determined this fraction using the pre-equilibrium spectra calculated with the PREEQ code for all ejectile types. The

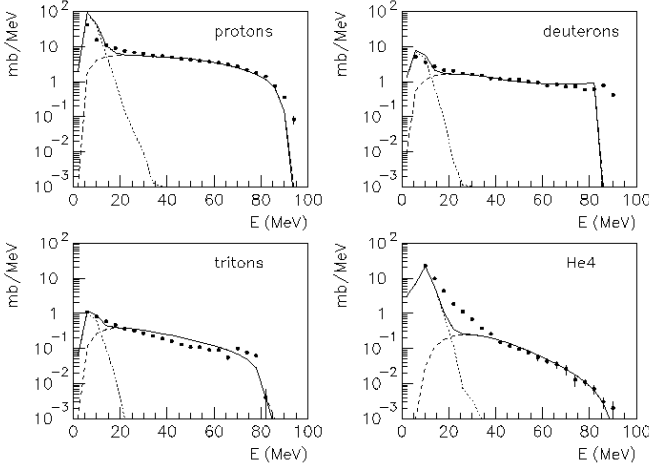


FIG. 27: Calculated pre-equilibrium and evaporation contributions (dashed and dotted lines respectively) in the particle emission spectra for the 96 MeV $^{56}\text{Fe}(n, Xlcp)$ reaction, compared to the experimental results of the present work (full circles). The calculated total distributions (sum of pre-equilibrium and evaporation spectrum) are presented as continuous lines.

resulting value obtained for the 96 MeV $^{56}\text{Fe}(n, X)$ reactions is $f_{PE}(E)=0.993$, in agreement with that estimated for 62 MeV $^{54}\text{Fe}(p, X)$ reactions in Ref. [31]. That value very close to 1 shows that almost the entire reaction cross section is available for the pre-equilibrium emission, and that the evaporation process of a compound nucleus represents a very small component with an associated value of $f_{EQ}(E)=0.007$. The second source of the equilibrium component which can be considered is the evaporation from a residual nucleus left in an excited state just after the pre-equilibrium emission has occurred. In order to estimate the excitation energy of such a nucleus and its formation probability after the pre-equilibrium emission of each outgoing particle type, again, we used the energy differential distributions previously calculated with PREEQ. The residual nucleus excitation energy is given by the formula $U=E-B_{\beta}-e_{\beta}$, where B_{β} and e_{β} are the binding energy of the emitted particle β and its emission energy respectively and E is the excitation energy of the compound nucleus. Having determined that quantity, the evaporation spectra are further calculated using the Hauser-Feshbach formalism [32]. Particles are emitted until the evaporation process is no longer energetically possible and the nucleus remaining energy is released in the form of gamma rays.

The results obtained for the 96 MeV $^{56}\text{Fe}(n, Xlcp)$ reactions are given in Fig. 27 (dotted lines), together with the pre-equilibrium component calculated with PREEQ as described in subsection A (dashed lines). The total particle emission spectrum determined by summing both mechanism contributions (continuous line) is also presented and compared to the experimental data

(points). The agreement found over the full energy range is relatively good, except for helium isotopes around 20 MeV, where the calculated distributions are below the experimental results. The same effect has been found for the $^{208}\text{Pb}(n, X^4\text{He})$ reaction, showing that the pre-equilibrium contribution for helium isotopes is underestimated in this energy region for both light and heavy targets. For hydrogen isotopes the introduction of the evaporation contribution allows a good description of the particle emission over a wide energy range.

D. Angular distributions

To complete our analysis about the models, we would like to compare the experimental angular differential cross sections to the theoretical ones. While the exciton model is largely used to calculate angle integrated energy spectra, the determination of angular distributions is out of its capabilities. In order to overcome this difficulty, several approaches involving modifications of the exciton model have been proposed, like in Ref. [33]. However, most of them contain serious approximations or induce computational complexities and they can be applied only for a limited set of reaction configurations. For this reason, a phenomenological approach proposed in Ref. [16] is often preferred to study the continuum angular distributions. It is based on a systematical study of a wide variety of experimental data. The parameterization established for the double-differential cross section as a function of the total energy-differential cross section is given by the equation:

$$\frac{d^2\sigma}{d\Omega de} = \frac{1}{4\pi} \frac{d\sigma}{de} \frac{a}{\sinh(a)} [\cosh(a\cos\theta) + f_{PE}\sinh(a\cos\theta)] \quad (3)$$

In this expression, θ is the emission angle in the center of mass frame, and the term a is the slope parameter depending on the incident particle type and energy, the target nucleus and the exit channel. It can be calculated using the procedure described in Ref. [16]. The f_{PE} parameter is the fraction of particle emission apart from equilibrium. It will be called further the fraction of pre-equilibrium emission and it is calculated using the formula:

$$f_{PE} = \frac{(d\sigma/de)_{PE}}{(d\sigma/de)} = \frac{(d\sigma/de)_{PE}}{(d\sigma/de)_{PE} + (d\sigma/de)_{EQ}} \quad (4)$$

where the PE and EQ symbols refer respectively to pre-equilibrium and equilibrium emissions. Using the energy-differential cross sections for these two processes calculated in subsections A and C, the double-differential cross sections are calculated according to equation (3). In Fig. 28 are presented the resulting angular distributions (lines) obtained for the proton emission in $^{56}\text{Fe}(n, X)$ and $^{208}\text{Pb}(n, X)$ reactions at 96 MeV (right and left figures respectively), together with the experimental data (points).

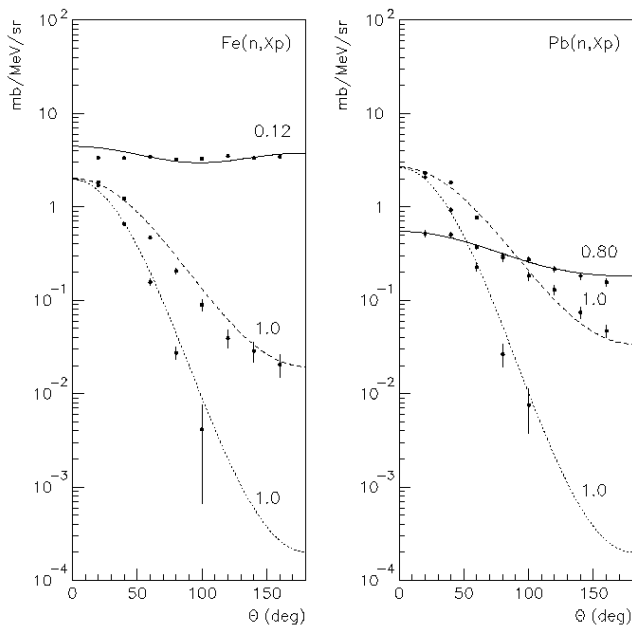


FIG. 28: Double-differential distributions calculated using the parameterization from Ref. [16] (lines) for proton emission in 96 MeV neutron-induced reactions on ^{56}Fe and ^{208}Pb compared with the experimental results (points). The continuous, dashed and dotted lines correspond to the 8–12 MeV, 40–44 MeV and 68–72 MeV emission energy ranges respectively. The contribution of the pre-equilibrium emission in the total cross section (f_{PE} factor) for each domain is also given near the corresponding distribution.

In order to have a better illustration of the different reaction mechanisms which contribute to the particle emission spectra (evaporation and pre-equilibrium emission), when we constructed the angular distributions, we chose three different energy domains: 8–12 MeV (continuous lines), 40–44 MeV (dashed lines) and 68–72 MeV (dotted lines). The contribution of the pre-equilibrium emission in the total cross section (f_{PE} factor) for each domain is also given near the corresponding distribution.

We observe in general satisfactory agreement between the theoretical results and the experimental distributions. At low energies (8–12 MeV), particles are emitted from both evaporation and pre-equilibrium processes whose respective contributions depend on the target nucleus mass. For the iron case, we found $f_{PE}=0.12$ and we observe a quasi-isotropic distribution, both signals indicating that the evaporation process is dominant for light targets. For the lead target, $f_{PE}=0.80$ and the angular distribution is slightly forward peaked, showing that low energy particles are mainly emitted during the pre-equilibrium stage. For more energetic particles, $f_{PE}=1$ for both targets, and we observe that they are mainly emitted at small angles, following the beam direction. From this, we deduce that those ejectiles are emitted before an equilibrium has been reached. We found a similar agreement when we built the complex particle dis-

tributions, showing that the Kalbach parameterization is able to give a proper description of the double differential cross sections, whatever the target or the emitted particle are. In addition, a physical basis for this parameterization has been established in Ref. [34], allowing a more detailed theoretical understanding of the properties of the angular distributions in the continuum energy domain.

VI. SUMMARY

In this paper, we report a new set of experimental data concerning light charged-particle production in 96 MeV neutron-induced reactions on natural iron, lead and uranium targets. Double-differential cross sections of charged particles have been measured over a wide angular range (20–160 degrees). With the MEDLEY set-up, data were measured for p, d, t, ^3He and alpha particles, with low energy thresholds. The SCANDAL set-up has been used to measure proton production cross sections in the same angular range, with good statistics and angular resolution, but with an energy threshold of about 30 MeV. For proton emission, the very good agreement found between both sets of measurements obtained with both independent detection systems shows that we had a good control on the systematical uncertainties involved. This is due, in part, to the unambiguous cross section normalization which has been applied using very accurate data on the np scattering cross section [13]. In our experiment, we also measured this cross section and we obtained a good agreement with data from Ref. [13]. The estimated systematical uncertainties affecting the double differential cross sections reported in this work are of the order of 5 %.

Data presented in this paper allows the extension to higher energies (up to 96 MeV) of the available experimental results on nucleon-induced reactions in the 20–200 MeV energy range, which were up to now limited to about 60 MeV incident energy. This new data set, together with the data already existing in the literature, allows us to study in detail both main theoretical approaches [3, 4] available nowadays for the description of nucleon and complex particle emission in nucleon-induced reactions at intermediate energies. These approaches have been proposed mainly to improve the exciton model predictions concerning the production of clusters, which was originally strongly underestimated by the model, as shown with the calculations we have performed with the GNASH code [6]. Since the cross sections evaluated with GNASH are at present implemented in the MCNPX code, we would like to issue a warning that some important information needed in specific application as the power deposited in a spallation target of an ADS could be underestimated.

In order to test both approaches, we performed calculations with the PREEQ [20] and PRECO-2000 [27] codes. The PREEQ results have shown that by taking

into account the cluster formation probability in the pre-equilibrium stage of the reaction, one can obtain a global agreement over a wide set of configurations. The formation probability is a free parameter in the PREEQ code and we have adjusted it for each target nucleus. The evolution of the resulting values shows that, for a given outgoing particle, the probability decreases with the target mass. In addition, for a given target, the formation probability is larger for lighter particles. This parameter depends very little on the incident particle type and energy. Proposed as an alternative to this approach, the method used in the PRECO-2000 code and implemented in the more recent code TALYS [28] to calculate complex particle production cross sections, considers contribution of direct reactions in the outgoing spectra. In many cases, however, this approach does not lead to a good reproduction of the experimental distributions. Despite the acceptable agreement found in some particular situations, it can not be used for the moment in a global description of nucleon-induced reactions. This deficiency is due in part to the strong dependence of its predictions on the projectile type. It is our hope that the work performed at present in the development of the TALYS code will soon provide an improved version of this approach.

We have completed the description of the particle emission over the full energy range by adding the contribution of the evaporation process to the pre-equilibrium emission calculated using the PREEQ code. That calculation scheme has shown that for heavy targets, almost all particles are emitted during the pre-equilibrium stage of the reaction, while for light targets, a strong component from the evaporation process is present at low emission energy. In addition, the most important contribution in the equilibrium component originates from the decay of residual nuclei left in an excited state after the pre-equilibrium particle emission. Finally, we shown that a correct description of the energy-differential distributions and of the different mechanisms contributing to the total cross section allows to calculate double-differential cross sections by including also the parameterization from Ref. [16] for the angular distribution determination. The good reproduction of the shapes of the double-differential distributions that we obtained with this method, suggests

that theoretical models must provide at least a good description of the energy-differential cross sections. The parameterization established in Ref. [16] allows a more detailed study of the reaction with a rather satisfactory accuracy by allowing the prediction of the double differential distributions.

The results presented in this work show that the understanding of nucleon-induced reactions at these energies is far from complete. Two approaches are available in the framework of the exciton model for the description of cluster emission in these specific reactions and among them, only that based on the coalescence model seems to have a satisfactory predictive power. It is, however, based on a scale factor associated to the formation probability of complex particles which has to be adjusted to experimental data. Therefore, further theoretical progress must be done in this field in order to improve the existing theoretical approaches of the exciton model and to provide new models based on different considerations. An alternative has been recently proposed in this direction, which uses the wavelet technique to simulate the nuclear dynamics and whose results are very encouraging. They will constitute the subject of a future publication [35].

Acknowledgments

This work was supported by the European Community under the HINDAS project (contract No. FIKW-CT-2000-0031), the GDR GEDEON (research group CEA-CNRS-EDF-FRAMATOME), Vattenfall AB, the Swedish Nuclear Fuel and Waste Management Company, the Swedish Nuclear Power Inspectorate, Barsebäck Power AB, Ringhals AB, the Swedish Defence Research Agency and the Swedish Research Council. We would like to thank the TSL staff for assistance and quality of the neutron beam. We are also grateful to Dr. E. Betak for very useful discussions concerning calculations with the PREEQ code. Special thanks to Dr. C. Kalbach for her thirty years of effort which have contribute significantly to the progress of theory in nucleon-induced reactions.

-
- [1] HINDAS: High and Intermediate energy Nuclear Data for Accelerator-driven Systems, European Community, Contract No. FIKW-CT-2000-0031
 - [2] J. J. Griffin, *Phys. Lett.* 17, 478 (1966)
 - [3] I. Ribanský and P. Obložinský, *Phys. Lett.* 45B, 318 (1973)
 - [4] C. Kalbach, *Z. Phys. A* 283, 401 (1977)
 - [5] J. R. Wu and C. C. Chang, *Phys. Rev. C* 17, 1540 (1978)
 - [6] P. G. Young, E. D. Arthur, and M. B. Chadwick, *Comprehensive Nuclear Model Calculations: Introduction to the Theory and Use of the GNASH Code*, LA-12343-MS (1992)
 - [7] A. N. Smirnov, V. P. Eismont and A. V. Prokofiev, *Rad. Meas.* 25, 151 (1995)
 - [8] S. Dangtip, A. Ataç, B. Bergenwall, J. Blomgren, K. Elmgren, C. Johansson, J. Klug, N. Olsson, G. Alm Carlsson, J. Söderberg, O. Jonsson, L. Nilsson, P.-U. Renberg, P. Nadel-Turonski, C. Le Brun, F.-R. Lecolley, J.-F. Lecolley, C. Varignon, Ph. Eudes, F. Haddad, M. Kerveno, T. Kirchner and C. Lebrun, *Nucl. Instr. Meth. A* 452, 484 (2000)
 - [9] J. Klug, J. Blomgren, A. Ataç, B. Bergenwall, S. Dangtip, K. Elmgren, C. Johansson, N. Olsson, S. Pomp,

- A.V. Prokofiev, J. Rahm, U. Tippawan, O. Jonsson, L. Nilsson, P.-U. Renberg, P. Nadel-Turonski, A. Ringbom, A. Oberstedt, F. Tovesson, V. Blideanu, C. Le Brun, F.-R. Lecolley, J.-F. Lecolley, M. Louvel, N. Marie, C. Schweitzer, C. Varignon, Ph. Eudes, F. Haddad, M. Kerveno, T. Kirchner, C. Lebrun, L. Stuttgé, I. Slypen, A. N. Smirnov, R. Michel, S. Neumann and U. Herpers, Nucl. Instr. Meth. A489, 282 (2002)
- [10] H. Condé, S. Hultqvist, N. Olsson, T. Rönnqvist, R. Zorro, J. Blomgren, G. Tibell, A. Håkansson, O. Jonsson, A. Lindholm, L. Nilsson, P.-U. Renberg, A. Brockstedt, P. Ekström, M. Österlund, F. P. Brady and Z. Szefflinski, Nucl. Instr. Meth. A292, 121 (1990)
- [11] J. F. Ziegler, *The Stopping and Range of Ions in Solids*, Pergamon Press, Elmsfor, New York, 1985
- [12] GEANT Detector Description and Simulation Tool, CERN Program Library Long Writeup W5013
- [13] J. Rahm, J. Blomgren, H. Condé, S. Dangtip, K. Elm-gren, N. Olsson, T. Rönnqvist, R. Zorro, O. Jonsson, L. Nilsson, P.-U. Renberg, A. Ringbom, G. Tibell, S. Y. van der Werf, T. E. O. Ericson and B. Loiseau, Phys. Rev. C63, 044001 (2001)
- [14] P. W. Lisowski, R. E. Shamu, G. F. Auchampaugh, N. S. P. King, M. S. Moore, G. L. Morgan, and T. S. Singleton, Phys. Rev. Lett. 49, 255 (1982)
- [15] T. Rönnqvist, H. Condé, E. Ramström, R. Zorro, J. Blomgren, A. Håkansson, A. Ringbom, G. Tibell, O. Jonsson, L. Nilsson, P.-U. Renberg, S. Y. van der Werf, W. Unkelbach and F. P. Brady, Nucl. Phys. A563, 225 (1993)
- [16] C. Kalbach, Phys. Rev. C37, 2350 (1988)
- [17] A. Guertin, N. Marie, S. Auduc, V. Blideanu, Th. Delbar, Ph. Eudes, Y. Foucher, F. Haddad, T. Kirchner, Ch. Le Brun, C. Lebrun, F.-R. Lecolley, J.-F. Lecolley, X. Ledoux, F. Lefèbvres, M. Louvel, A. Ninane, Y. Patin, Ph. Pras, G. Rivière and C. Varignon, to be published
- [18] H. Machner, Phys. Lett. 86B, 129 (1979)
- [19] K. K. Gudima, S. G. Mashnik and V. D. Toneev, Nucl. Phys. A401, 329 (1983)
- [20] E. Betak, Comp. Phys. Comm. 9, 92 (1975)
- [21] GEANT4 Physics Reference Manual, <http://wwwasd.web.cern.ch/wwwasd/geant4/geant4.html>
- [22] F. E. Bertrand and R. W. Peele, Phys. Rev. C8, 1045 (1973)
- [23] M. Blann, R. R. Doering, A. Galonski, D. M. Patterson and F. E. Serr, Nucl. Phys. A257, 15 (1976)
- [24] H. Machner, Phys. Rev. C21, 2695 (1980)
- [25] T. C. Awes, G. Poggi, C. K. Gelbke, B. B. Back, B. G. Glagola, H. Breuer and V. E. Viola, Jr., Phys. Rev. C24, 89 (1981)
- [26] H. H. Gutbrod, A. Sandoval, P. J. Johansen, A. M. Poskanzer, J. Gosset, W. G. Meyer, G. D. Westfall and R. Stock, Phys. Rev. Lett. 37, 667 (1976)
- [27] C. Kalbach-Walker, Users Manual for PRECO-2000 (2001)
- [28] A. Koning, unpublished
- [29] M. Kerveno, F. Haddad, Ph. Eudes, T. Kirchner, C. Lebrun, I. Slypen, J. P. Meulders, C. Le Brun, F. R. Lecolley, J. F. Lecolley, M. Louvel, F. Lefbvres, S. Hilaire and A. J. Koning, Phys. Rev. C66, 014601 (2002)
- [30] J. R. Wu and C. C. Chang, Phys. Rev. C16, 1812 (1977)
- [31] J. R. Wu and C. C. Chang, Phys. Lett. 60B, 423 (1976)
- [32] W. Hauser and H. Feshbach, Phys. Rev. 87, 366 (1952)
- [33] G. Mantzouranis, D. Agassi and H. A. Weidenmüller, Phys. Lett. 57B, 220 (1975)
- [34] M. B. Chadwick and P. Obložinský, Phys. Rev. C50, 2490 (1994)
- [35] F. Sébille, C. Bonilla, V. Blideanu and J.-F. Lecolley, to be published